A test of basin-scale acoustic thermometry using a large-aperture vertical array at 3250-km range in the eastern North Pacific Ocean

Peter F. Worcester, Bruce D. Cornuelle, Matthew A. Dzieciuch, and Walter H. Munk
Scripps Institution of Oceanography, University of California at San Diego, La Jolla, California 92093

Bruce M. Howe, James A. Mercer, and Robert C. Spindel
Applied Physics Laboratory, University of Washington, Seattle, Washington 98105

John A. Colosi
Woods Hole Oceanographic Institution, Woods Hole, Massachusetts 02543

Kurt Metzger and Theodore G. Birdsall
Communications and Signal Processing Laboratory, Electrical Engineering and Computer Science Department, University of Michigan, Ann Arbor, Michigan 48109

Arthur B. Baggeroer
Massachusetts Institute of Technology, Cambridge, Massachusetts 02139

(Received 12 November 1997; revised 14 January 1999; accepted 5 March 1999)

Broadband acoustic signals were transmitted during November 1994 from a 75-Hz source suspended near the depth of the sound-channel axis to a 700-m long vertical receiving array approximately 3250 km distant in the eastern North Pacific Ocean. The early part of the arrival pattern consists of raylike wave fronts that are resolvable, identifiable, and stable. The later part of the arrival pattern does not contain identifiable raylike arrivals, due to scattering from internal-wave-induced sound-speed fluctuations. The observed ray travel times differ from ray predictions based on the sound-speed field constructed using nearly concurrent temperature and salinity measurements by more than *a priori* variability estimates, suggesting that the equation used to compute sound speed requires refinement. The range-averaged ocean sound speed can be determined with an uncertainty of about 0.05 m/s from the observed ray travel times together with the time at which the near-axial acoustic reception ends, used as a surrogate for the group delay of adiabatic mode 1. The change in temperature over six days can be estimated with an uncertainty of about 0.006 °C. The sensitivity of the travel times to ocean variability is concentrated near the ocean surface and at the corresponding conjugate depths, because all of the resolved ray arrivals have upper turning depths within a few hundred meters of the surface. © *1999 Acoustical Society of America.* [S0001-4966(99)04506-3]

PACS numbers: 43.30.Pc, 43.30.Cq [SAC-B]

INTRODUCTION

Broadband acoustic signals were transmitted during November 1994 from a 75-Hz source to a 700-m-long vertical line array of hydrophones approximately 3250 km distant in the eastern North Pacific Ocean as part of the Acoustic Engineering Test (AET) of the Acoustic Thermometry of Ocean Climate (ATOC) project. The overall goals were (*i*) to determine the accuracy with which gyre- and basin-scale ocean temperature and heat content variability can be measured using the methods of ocean acoustic tomography, (*ii*) to determine the vertical resolution that can be obtained at multimegameter range in a single vertical slice containing an acoustic source and receiver, and (*iii*) to understand the influences that smaller-scale processes like internal waves and mesoscale eddies have on the signals. This paper focuses on the accuracy and resolution with which gyre-scale temperature and heat content can be measured using acoustic methods. A companion paper by Colosi *et al.* (1999) focuses on internal-wave effects and the potential predictability of these effects using analytic acoustic fluctuation theories based on internal-wave dominance.

A number of previous experiments have firmly established the accuracy and resolution with which tomographic methods can measure ocean temperature and current at ranges of up to about 1000 km (Munk *et al.*, 1995). There have been only a few previous experiments in which broadband acoustic signals have been transmitted over multimegameter ranges, however, and these experiments have left a number of issues unresolved, as discussed below.

In an experiment conducted intermittently from 1983-1989, a broadband 133-Hz source mounted on the bottom at 183-m depth near Kaneohe, Hawaii, transmitted roughly 3.7 Mm to a bottom-mounted horizontal array at 1433-m depth offshore of California [see Spiesberger and Tappert (1996), and the papers referenced therein]. Interpretation of the received signals was complicated because all of the energy reflected one or more times from the slope near Oahu before becoming trapped in the sound channel. No individual, re-

solved ray arrivals were observed. Rather, five distinct and relatively stable arrivals found near the beginning of complex receptions lasting several seconds were shown to be ray arrival *clusters*, each containing many predicted ray arrivals. All five ray clusters consisted of steep rays inclined at about 15° to the horizontal at the depth of the sound-channel axis. The accuracy of the interpretation of the observed travel-time variability of the ray clusters purely in terms of ocean temperature changes is somewhat uncertain. As ocean conditions change, the locations at which the rays interact with the bottom will change. The bathymetry at the locations ensonified by the rays is not well known, and so the extent to which changes in path length of the bottom-reflected rays might be contributing to the observed travel-time changes is also uncertain.

A second experiment conducted in 1987 showed that individual ray arrivals associated with very steep ray paths are resolvable, identifiable, and stable at 3-4-Mm ranges, when bottom interactions are unimportant. In this experiment, transmissions from a broadband 250-Hz source moored near the depth of the sound-channel axis in the central North Pacific Ocean (Dushaw *et al.*, 1993) to a bottom-mounted horizontal array in deep water about 3 Mm distant were analyzed in detail (Spiesberger and Metzger, 1991; Spiesberger *et al.*, 1994). All of the measured arrivals for this transmission path corresponded to rays that either reflected from the surface or had upper turning depths within a few tens of meters of the surface. As a result the vertical resolution that might have been achievable using a receiver located closer to the depth of the sound-channel axis could not be determined. Interpretation of the absolute travel times in this experiment was difficult because the locations of the source and receiver were not precisely known and because no measurements were made of the sound-speed field between the source and receiver at the time of the experiment.

Finally, the Heard Island Feasibility Test (HIFT) in January 1991 demonstrated that low-frequency coded transmissions with a center frequency of 57 Hz could be coherently processed to yield adequate signal-to-noise ratios (SNRs) at ranges of up to 18 Mm (Munk *et al.*, 1994). None of the HIFT receptions yielded arrivals that were resolvable and identifiable with specific rays or modes, even at ranges as short as 5 Mm. Given that the previous experiments discussed above had yielded either ray clusters or individual ray arrivals that were identifiable at 3-4-Mm ranges, the inability to identify specific arrivals at about 5-Mm range in the HIFT case was probably due in part to the fact that all the signals traversed the complex oceanographic structure associated with the Antarctic Circumpolar Front. The difficulties encountered in interpreting the observed receptions were exacerbated by the fact that the sources were suspended from a moving ship, so that the geometry was continually changing and the long-term stability of the transmissions could not be determined.

The ATOC Acoustic Engineering Test differed from these earlier experiments in a number of important ways. Both the 75-Hz source and the receiver were located near the depth of the sound-channel axis at deep-ocean locations to avoid bottom interactions. The receiver was a 700-m-long vertical line array so that the vertical structure of the received signals could be measured. One implication is that the vertical arrival angles of any raylike arrivals could be determined and used to confirm the ray identifications. Further, the array was designed to be able to spatially resolve the low order acoustic modes, so that modal travel times could be measured and modal scattering studied. The locations of the source and receiver were precisely determined using GPS navigation, so that the absolute range is known to within a few meters. Finally, the temperature and salinity fields along the transmission path connecting the source and receiver were measured during the experiment with closely spaced expendable bathythermograph (XBT) and expendable conductivity-temperature-depth (XCTD) casts, so that the upper-ocean sound-speed field can be accurately computed.

We are unaware of any previous broadband measurements that have been made at ranges in excess of 1000 km with a vertical receiving array. A long vertical array was deployed off Monterey, California, during HIFT at a range of 17 Mm to measure the modal content of the received signals, but low SNRs precluded broadband processing (Baggeroer *et al.*, 1994). Narrowband analyses showed a surprisingly rich modal population. The experiment that most closely resembles the one described here occurred during July 1989, when broadband signals were transmitted from a moored 250-Hz source to a 3-km-long vertical receiving array 1000 km distant in the north central Pacific Ocean (Howe *et al.*, 1991; Duda *et al.*, 1992; Cornuelle *et al.*, 1993; Worcester *et al.*, 1994). This experiment showed that energy confined near the sound-channel axis is significantly scattered by small-scale oceanic variability, reducing the vertical resolution that can be obtained using tomographic methods (Colosi *et al.*, 1994).

The ATOC Acoustic Engineering Test is described in Sec. I of this paper. The measured broadband acoustic arrival pattern at 3250-km range and 75-Hz center frequency is then compared in Sec. II with the arrival pattern predicted using the nearly concurrent temperature and salinity measurements. The goal is to determine if the two are quantitatively consistent as a function of travel time and depth to within the uncertainty imposed by our necessarily incomplete knowledge of the sound-speed field. A full and complete understanding of the forward problem is the *sine qua non* of any inverse problem. The observed ray travel times are found to differ from ray predictions by more than *a priori* variability estimates, suggesting that the equation used to compute sound speed from temperature, salinity, and pressure requires refinement. One of the key issues is the extent to which near-axial acoustic energy is scattered by internal-wave-induced sound-speed fluctuations. It is conceivable that acoustic scattering from small-scale oceanic variability will set a maximum range beyond which it is impossible to extract meaningful information on the temperature of the intervening ocean from acoustic travel-time data. Linear inverse methods are used in Sec. III to estimate the accuracy and vertical resolution with which the sound-speed field (and therefore temperature and heat content) in the vertical plane containing the source and receiver can be determined at mul-

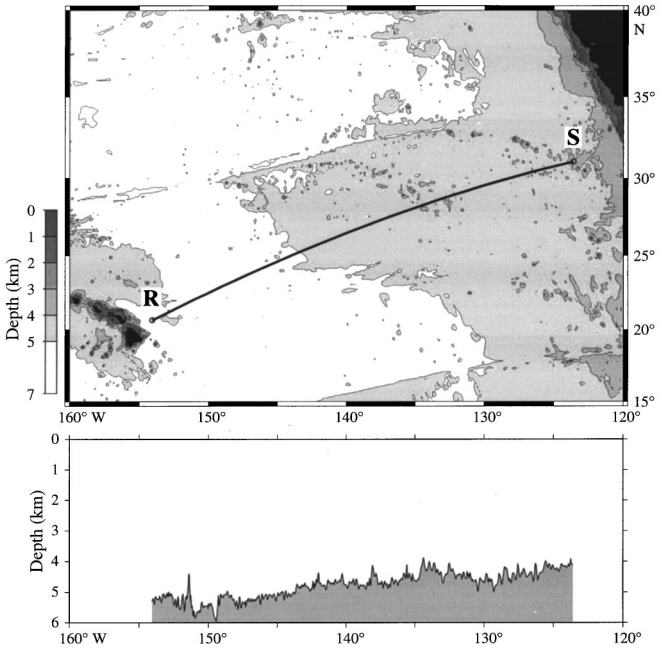

FIG. 1. Acoustic path from the 75-Hz acoustic source **S** suspended from R/P FLIP to the vertical receiving array **R** moored east of Hawaii. The path is superimposed on ETOPO-5 bathymetry (National Geophysical Data Center, 1988). Neither the ETOPO-5 bathymetry nor an improved estimate of the bathymetry using satellite altimetry data (bottom) shows significant features along the acoustic path. The improved bathymetry was derived by combining conventional sounding data with depths estimated from the gravity anomaly field computed from satellite altimetry data (Smith and Sandwell, 1994; Sandwell and Smith, 1997; Smith and Sandwell, 1997).

timegameter ranges. Finally, in Sec. IV we discuss the implications of these results.

I. THE EXPERIMENT

The acoustic source was suspended at 652-m depth, near the sound-channel axis, from the floating instrument platform R/P FLIP, which was moored in the eastern North Pacific Ocean at 31° 2.050′N, 123° 35.420′W, in water more than 4000 m deep (Fig. 1). R/P FLIP was in a trimoor to minimize source motion. The transmissions were received on two autonomous vertical line array (AVLA) receivers, as well as on numerous U.S. Navy receivers in the North Pacific Ocean and on a deep sonobuoy receiver near New Zealand. The results presented here were obtained from the AVLA moored at 20° 39.040′N, 154° 04.640′W, just east of Hawaii, in water about 5312 m deep. The source and receiver positions were determined to within a few meters using differential GPS navigation. The range was 3 252 382 m (WGS-84). The refracted geodesic, which includes the effects of horizontal gradients in sound speed (see Munk *et al.*, 1995), is separated from the unrefracted geodesic by less than 2 km along the entire path and is longer than the unrefracted geodesic by only about 3 m. The transmission path does not cross any major oceanographic fronts or other features. There are no significant bathymetric features along the path (Fig. 1).

The instrumentation and signal processing are described in detail by the ATOC Instrumentation Group (1995). Only a brief summary is given here.

The source transmitted a phase-modulated signal with a center frequency of 75 Hz. The phase modulation was encoded using a linear maximal-length shift-register sequence containing 1023 digits. The source transducer has less bandwidth than desired but more drive capability than needed. The input waveform used to drive the source was therefore adjusted to give an output signal containing phase-modulated digits with two cycles of carrier each, even though the inherent bandwidth of the source was significantly narrower than $Q=2$ (37.5 Hz). Each digit was then 26.667 ms in duration, and each sequence period was 27.2800 s long. Fifty-four transmissions were made, consisting of a mix of 10-, 20-, and 40-min transmissions, with 2 to 4 h between transmissions. The source level was 260 W (195 dB *re* 1 μPa at 1 m).

The vertical receiving array consisted of 20 hydrophones at 35-m spacing (1.75 wavelengths at 75 Hz) between 900- and 1600-m depth. (A second 20-hydrophone subarray, between 200- and 900-m depth, failed.) The incoming hydrophone signals were amplified, bandpass filtered, and sampled using 16-bit analog-to-digital converters at a 300-Hz rate.

Transmissions were made for seven days during November 1994, beginning on yearday 321 (17 November 1994) and ending on yearday 327 (23 November 1994). After return to shore, the acoustic data were complex demodulated and the phase modulation was removed. Forty periods (1091.20 s) of the received signal were recorded for the 20-min transmissions, but only 28 periods (763.840 s) were coherently processed to form the receptions shown here. The SNR of the ray arrivals did not increase for longer averaging times, indicating that the signal duration exceeded the signal coherence time. Doppler processing was required owing to the relative velocities of the moored source and receiver. Even though the relative velocities were small (1-2 cm/s), the long coherent processing time made the relative motion during transmissions significant. A standard Doppler search was performed for each reception to determine the relative velocity (assumed constant) that yielded the maximum output signal level.

The position of the source and the position and shape of the AVLA were measured by long-baseline acoustic navigation systems, using acoustic transponders on the seafloor. The source's position was determined to within about 1 m rms, using acoustic interrogators on the source package and on R/P FLIP. Source displacements as large as 1500 m occurred, with typical velocities of 1-2 cm/s (Fig. 2). The absolute positions of the elements in the vertical receiving array were determined to within about 1.5-m rms, using an acoustic interrogator at the center of the array. The navigation signals were received on six of the same hydrophones used to receive the 75-Hz signals, distributed over the array aperture, as well as on the interrogation transducer. The relative positions of the hydrophones were determined to within about 0.2 m rms. Array displacements in excess of 100 m were observed, as well as significant array curvature (Figs. 2 and 3).

Surprisingly, the relative velocities determined from the measured source and receiver locations did not always agree with those determined from the Doppler processing. The discrepancy is due to acoustic travel-time (phase) changes pro-

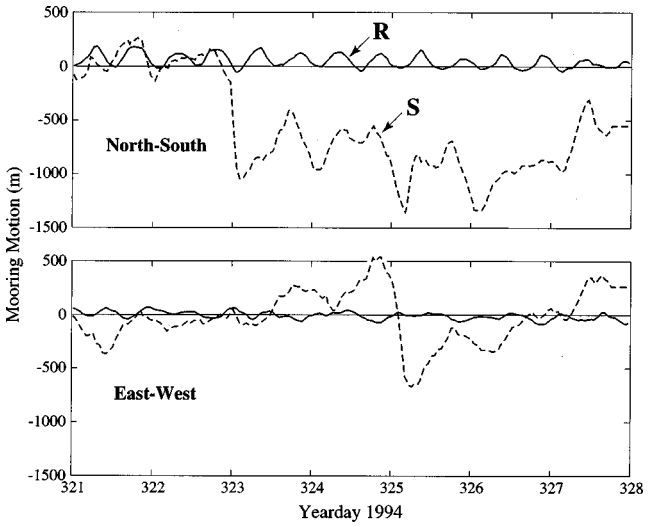

FIG. 2. North-south and east-west displacements of the source **S** (dashed) and of the center of the vertical receiving array **R** (solid) versus time.

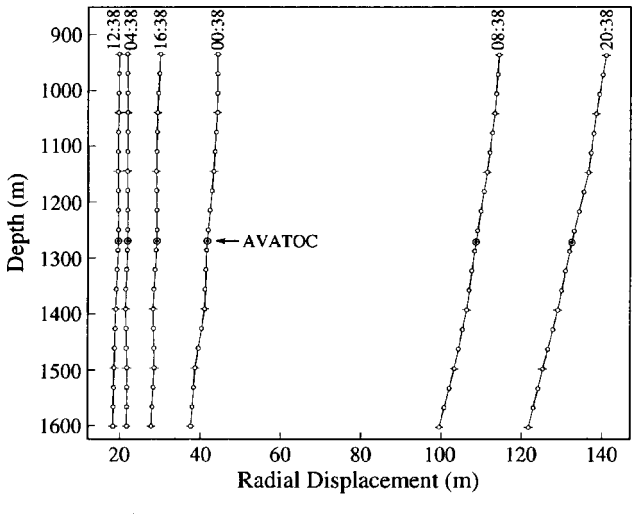

FIG. 3. Radial displacement of the Hawaii AVLA on yearday 326, 1994. All times are UTC.

duced during a transmission by the change in the barotropic tidal current along the acoustic path over the 20-min transmission interval. (Constant velocities, even if range dependent, do not produce a Doppler shift.) Tidally induced phase changes can be comparable to those caused by relative motions of the source and receiver. Even if both the source and receiver were truly fixed, a tidal correction would be required, either by Doppler processing or by a tidal prediction which allows for the finite duration of the transmission.

The temperature and salinity fields along the acoustic path were directly measured during the experiment. XBT (T-7) casts to 760-m depth were made at approximately 30-km intervals. XCTD casts to 1000-m depth were made at approximately 300-km intervals, in conjunction with every tenth XBT cast. The XBT/XCTD survey required seven days, from yearday 325 (21 November 1994) through yearday 331 (27 November 1994), and thus overlapped with the end of the transmission period. The survey began at the receiver and proceeded toward the source.

II. THE FORWARD PROBLEM: PREDICTABILITY OF ACOUSTIC PROPAGATION

The combination of a vertical receiving array, nearly concurrent environmental measurements, and broadband signals designed to measure acoustic travel times with a precision of a few milliseconds makes it possible to test quantitatively whether the measured arrival pattern is consistent with predictions to within measurement uncertainty. Plotting acoustic intensity as a function of travel time and hydrophone depth clearly reveals acoustic wave fronts sweeping across the array (Fig. 4). Wave fronts can be seen prior to a travel time of about 2195 s, after which the arrival pattern becomes quite complex.

A. Sound-speed field

The depth of the sound-channel axis gradually deepens as one proceeds from the source toward the receiving array (Fig. 5). Sound speeds were derived from climatological temperature (Levitus and Boyer, 1994) and salinity (Levitus *et al.*, 1994) data for November extracted from the World Ocean Atlas 1994. This climatology will be referred to hereafter as the WOA94 climatology, with the understanding that the climatology for November is used, rather than the annual average. Sound speeds were computed using the sound-speed equation of Del Grosso (1974). [Millero and Li (1994) provide a corrected version of the sound-speed equation of Chen and Millero (1977) that is equivalent for the parameter range of interest here and could equally well have been used.] The historical sound-channel axis is at about 650-m depth at the source and reaches about 800-m depth at the receiver, although the minima are not sharply defined. The source is therefore approximately on axis, and the top of the receiving array is slightly below axial depth.

Sound speeds in the upper 760 m at the time of the experiment were derived from the XBT and XCTD data. The

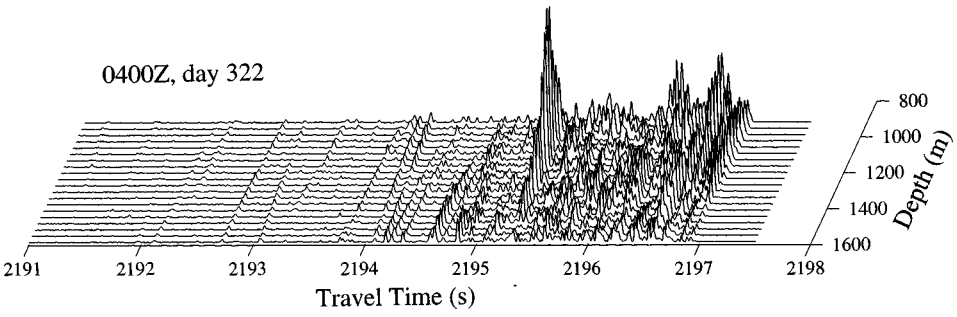

FIG. 4. Acoustic intensity as a function of travel time and hydrophone depth for the transmission at 0400 UTC on yearday 322.

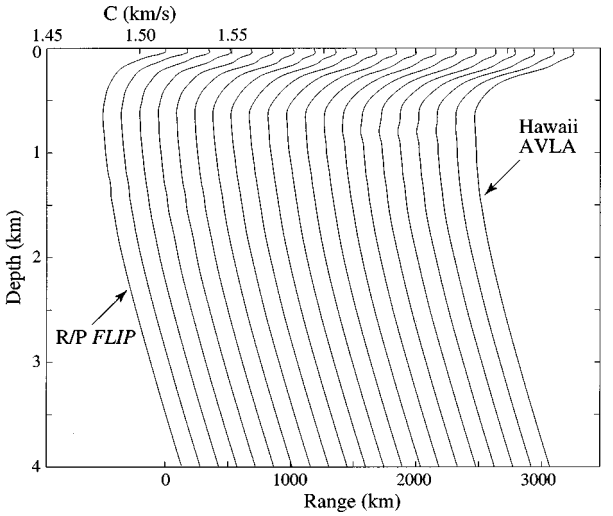

FIG. 5. Sound-speed profiles as a function of range between the source and receiving array, derived from the WOA94 climatology for November. Profiles are plotted every 162 km, corresponding to a sound-speed offset of 10 m/s.

salinity values corresponding to the XBT temperatures were estimated using the temperature-salinity relation from the nearest XCTD cast. Sound speeds below 760-m depth were calculated from the WOA94 climatology, as in Fig. 5. The upper ocean perturbations derived from the XBT/XCTD data were smoothed into the WOA94 sound-speed field below 760-m depth using a 200-m vertical *e*-folding scale.

A smooth, range-dependent sound-speed field was constructed from a combination of the XBT/XCTD measurements and the historical data by objective mapping (Fig. 6). The objective mapping procedure provides an estimate of the uncertainties in the smooth field due to limited coverage and measurement noise. These uncertainties can be converted into uncertainties for the travel-time predictions made from the objectively mapped field by using the linearized forward problem (Dushaw *et al.*, 1993; Cornuelle *et al.*, 1993). The objective mapping procedure also largely removes internal-wave variability from the sound-speed maps by smoothing in the horizontal and the vertical with scales appropriate to ocean mesoscale variability.

To construct the maps, the sound-speed field was expressed as a range-dependent perturbation field relative to a range-dependent reference field obtained from the WOA94 climatology. The sound-speed perturbation was assumed to

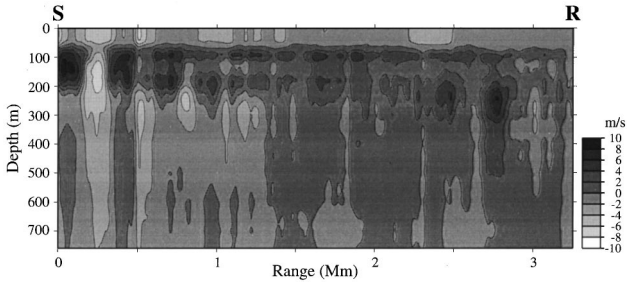

FIG. 6. Sound-speed perturbation in the upper 760 m computed by subtracting sound speeds derived from the WOA94 climatology from objectively mapped sound speeds derived from the XBT/XCTD data. The contour interval is 2 m/s. The source **S** is on the left and the receiver **R** is on the right.

be a random variable with zero mean and a known covariance, separable into an inhomogeneous vertical covariance and a homogeneous, depth-independent horizontal covariance with 70-km *e*-folding scale.

The sound-speed perturbation field $\Delta C(x,z)$ was discretized as a sum of products of horizontal and vertical functions,

$$\Delta C(x,z)=\sum_{j=1}^{M}\sum_{k=1}^{K} a_{jk}F_j(z)G_k(x), \tag{1}$$

where a_{jk} are the model parameters. The $F_j(z)$ were chosen to be the eigenvectors of the vertical covariance of the sound-speed perturbations as a function of depth as estimated from the XBT data,

$$\langle \Delta C(z_1)\Delta C(z_2)\rangle=\sum_{j=1}^{M} F_j(z_1)\lambda_j^2 F_j(z_2), \tag{2}$$

where the λ_j are the eigenvalues, i.e., the $F_j(z)$ are the empirical orthogonal functions (EOFs) for the XBT data set. The first six EOFs were used, which account for 93% of the observed XBT variance. Retaining additional EOFs only gradually reduces the residual variance while increasing the number of model parameters and the small-scale structure in the mapped field.

Truncated Fourier series were used for the horizontal parametrization. The wave number spectrum was specified to be white for wavelengths longer than 300 km, and proportional to wavelength (inverse wave number) squared for shorter wavelengths. This spectrum gives a horizontal covariance *e*-folding scale of 70 km but includes allowances for a strong mean component.

Sound speeds computed from the XBT/XCTD measurements, $C(x_i,z_i)$, are related to the model parameters by

$$\begin{aligned}\Delta C_i(x_i,z_i)&\equiv C(x_i,z_i)-C_0(x_i,z_i)\\ &=\sum_{j=1}^{M}\sum_{k=1}^{K} a_{jk}F_j(z_i)G_k(x_i)+r_i,\end{aligned} \tag{3}$$

where the ΔC_i are the sound-speed perturbations at the measurement locations relative to a reference sound-speed field $C_0(x_i,z_i)$, selected here to be the WOA94 climatology. The measurement noise r_i is due to instrument error (which varies with depth and is typically correlated because of fall-rate error) and unmodeled phenomena (model error), including internal waves. The coefficients a_{jk} are computed by objective mapping, i.e., by a tapered, weighted least-squares fit that minimizes the differences between the ΔC_i computed from the XBT data and those computed from the ocean model.

The sound-speed perturbation field shows significant eddy activity near the source, with peak perturbations of up to about 10 m/s (Fig. 6). The eddy activity is weaker over most of the remaining path. A more-or-less uniform surface mixed layer with a depth of about 100 m is present over almost the entire path.

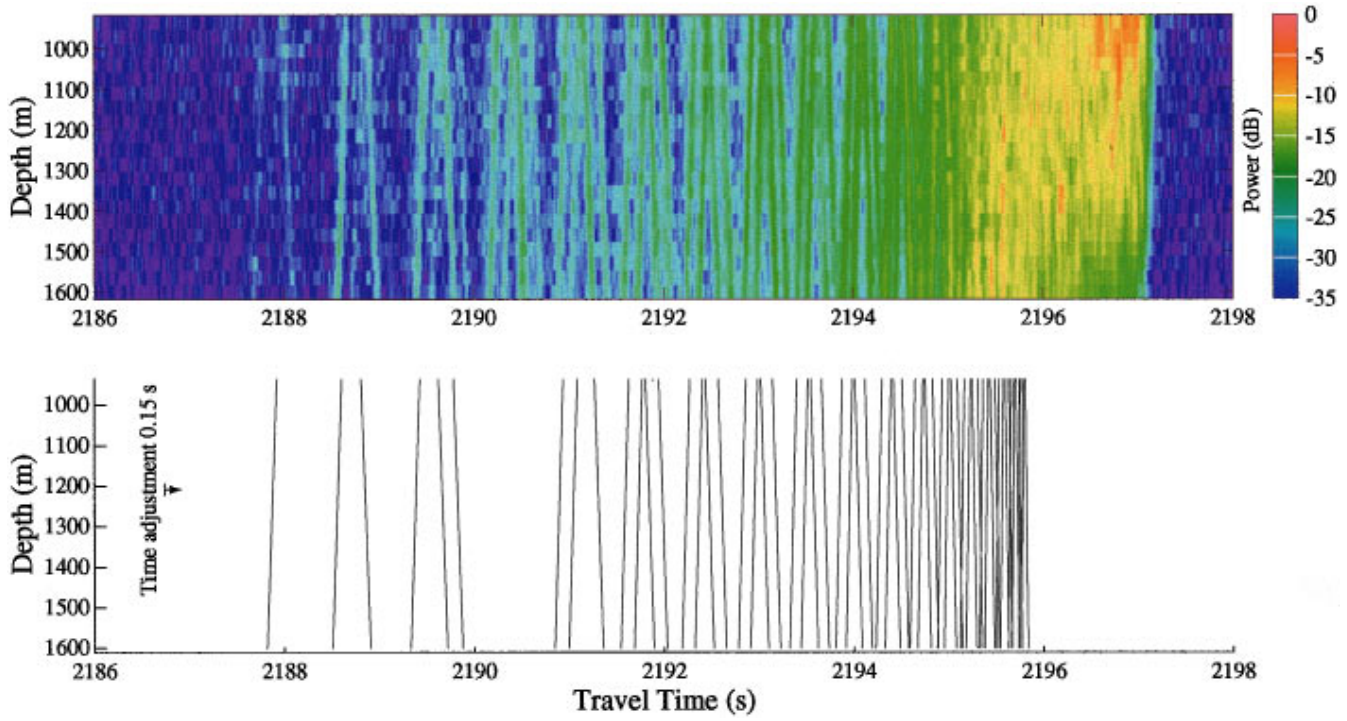

FIG. 7. (Top) Measured daily average acoustic intensity as a function of travel time and hydrophone depth. The measured pattern is an incoherent average of all of the receptions on yearday 326, 1994. Acoustic intensity relative to the peak intensity in the daily average is plotted in decibels. (Bottom) Predicted travel times versus hydrophone depth computed using a range-dependent ray tracing algorithm and the sound-speed field derived from the WOA94 climatology. Only the wave fronts predicted by ray theory prior to about 2196 s are shown. The predicted travel times have been delayed by 0.15 s to align the measured and predicted arrival patterns.

B. Geometric optics and ray identification

Raylike arrivals, in the form of wave fronts sweeping across the array, are clearly evident in the measured data prior to a travel time of about 2195 s, as noted above. These arrivals are both resolvable and stable over the duration of the experiment. It will be shown in this section (*i*) that these arrivals can be unambiguously identified with specific acoustic rays using any of several ocean climatologies, without the need to use the XBT/XCTD data, and (*ii*) that the measured travel times are offset from the travel times predicted using the sound-speed field constructed from the XBT/XCTD measurements by a surprisingly large amount.

Using the sound-speed field constructed from the WOA94 climatology, range-dependent ray tracing over the measured range between the source and receiver gives predicted wave fronts that match those observed (Fig. 7). The range-dependent ray code used is that of Colosi; the predicted travel times have been checked against those from RAY (Bowlin *et al.*, 1993). The ray tracing was done in Cartesian coordinates, after appropriately transforming the depth coordinate and sound-speed profiles from spherical coordinates (Munk *et al.*, 1995). The radius of curvature to be used in the transformation is not obvious, as the true radius of curvature is a function of position on a spheroidal earth. Changing the assumed radius of curvature by up to 50 km changes the computed travel times for the geometry of this experiment by less than 3 ms, however, so the precise choice of the radius of curvature is not critical.

The measured and predicted travel times do not agree exactly, of course, at least in part because the ocean sound-speed field at the time of the acoustic transmissions is not the same as that computed from the WOA94 climatology. The predicted travel times shown in Fig. 7 have been delayed by 0.15 s to approximately align the measured and predicted arrival patterns. The similarity of the measured and predicted arrival patterns makes the identification of the measured wave fronts with particular ray paths straightforward. At least in this case climatological data are adequate for ray identification. The essential information to be used in the inversions in Sec. III is the slight mismatch between the measured and predicted travel times. The significance of the overall shift between the two patterns will be discussed at length in that section.

The identification can be confirmed by comparing the measured and predicted vertical arrival angles of the rays (Fig. 8). The measured arrival angles were estimated from the data with a conventional plane-wave beamformer, using the entire 700-m array aperture. The predicted arrival angles were obtained from the same range-dependent ray trace used to construct Fig. 7. After shifting the predicted travel times 0.15 s later, as in Fig. 7, the agreement between the measured and predicted ray arrival times and angles is excellent. Each wave front can therefore be labeled with an identifier $\pm n$, where $+$ $(-)$ indicates a ray that initially travels upward (downward) at the source and has a total of n upper and lower turning points between the source and receiver. None of the identified rays interacts with the seafloor.

Given the large number of resolved wave fronts in the

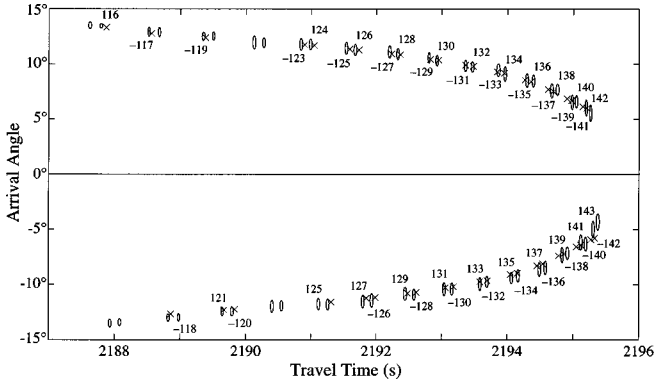

FIG. 8. Measured (ellipses) and predicted (crosses) vertical arrival angles versus travel time for the raylike arrivals. The ellipses are centered on the time-mean travel times of the ray arrivals for the entire experiment. The sizes of the ellipses show the rms variations in angle and time about the means. The predicted arrivals were computed using the WOA94 climatology and were delayed by 0.15 s to align the measured and predicted arrival patterns, as in Fig. 7. The arrivals are labeled with their ray identifiers.

measured arrival pattern, with similar vertical arrival angles, the ray identification might appear to be ambiguous. To test whether this is indeed the case, the rms difference between the measured and predicted travel-time patterns was computed as a function of the time shift applied to the predicted travel-time pattern (Fig. 9). To make this calculation, time series of the measured travel times for each ray arrival were constructed from the beamformer output (Fig. 10). The time-means of these series were then used to compute the rms travel-time difference. The rms difference has a clear global minimum for a time shift of 0.15 s, indicating that the measured and predicted time-mean patterns are most closely aligned when the predicted pattern is shifted later by this amount. (This is the shift used to align the measured and predicted arrival patterns in Figs. 7 and 8.) Sound speeds from the WOA94 climatology were used to construct Fig. 9. Similar results (Table I) were obtained using sound speeds computed from the earlier 1982 Levitus climatology (Levitus, 1982) and a climatology recently developed by Mem-

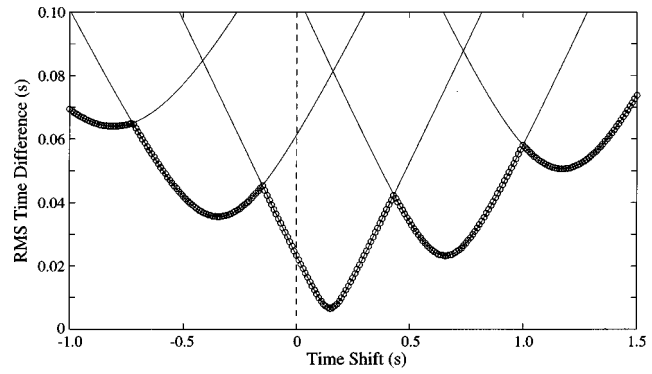

FIG. 9. The rms difference between the time means of the measured travel times for each ray arrival, as determined from the beamformer output, and the predicted travel times, versus the time shift applied to the predicted travel times to align the two patterns. The rms travel-time difference is normalized by the number of identified rays. The predicted arrivals were computed using the WOA94 climatology, as in Figs. 7 and 8. A positive time shift means that the predicted travel times are less than the measured travel times.

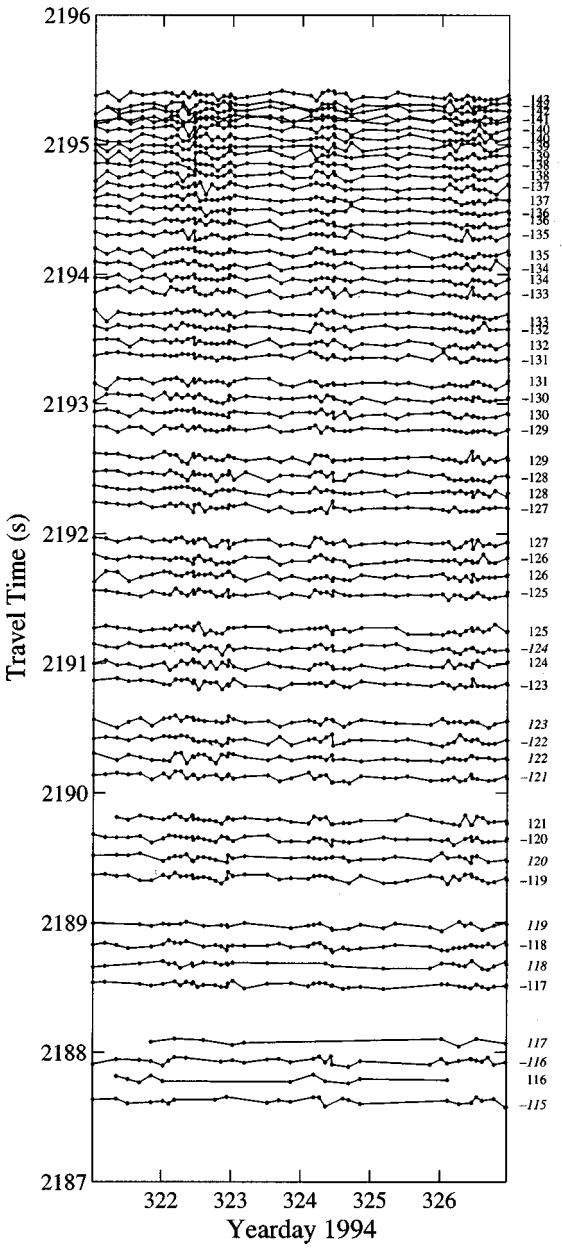

FIG. 10. Acoustic travel times for the raylike arrivals, as determined from the plane-wave beamformer output, versus yearday. The beamformer output is for an effective depth of 1268 m, the midpoint of the nominal array location. The travel times have been corrected for motion of the source and receiving array, as well as for clock drifts in the receiver. The source clock was synchronized to UTC using a GPS receiver. Ray identifiers are given on the right. Ray identifiers in italics indicate rays for which the ray trace code used did not succeed in locating the eigenray due to computational difficulties, although the identifications are nonetheless unambiguous.

emenlis *et al.* (1997). In all cases, the minimum is unique, so the ray identification is unambiguous.

The structure of the rms time difference as a function of time shift can be understood by noting that both the measured and predicted arrivals come in groups of four, as is evident in Fig. 7 (see, e.g., Munk *et al.*, 1995). Any ambiguity will therefore be in associating measured and predicted groups of four arrivals. The secondary minima in Fig. 9 occur when groups of four in the predicted pattern are associated with incorrect groups of four in the measured pattern.

Given an unambiguous ray identification, the discrep-

TABLE I. Comparison of the ray travel times predicted for various sound-speed fields with the time means of the measured travel times for each ray arrival, as determined from the beamformer output. The time shift that gives the best alignment between the predicted and measured travel times, the rms difference between the two for this time shift (normalized by the number of identified rays), and the number of identified rays are given. A positive time shift means that the measured travel times are greater than the predicted travel times.

	Time shift, (s)	rms, (s)	No. of identified rays
Levitus (1982)	0.01	0.0067	48
WOA94	0.15	0.0063	47
Menemenlis	0.01	0.0114	52
WOA94+XBT	0.22	0.0049	49

ancy between the measured and predicted ray arrival times can be quantified. Figure 11 shows the travel-time perturbation $\Delta\tau$ computed by subtracting the predicted travel times from the time-mean measured travel times, as derived from the plane-wave beamformer output. Predictions were made using both the sound-speed field derived from the WOA94 climatology and the objectively mapped sound-speed field derived from the XBT/XCTD data. The travel-time perturbations are plotted as a function of the minimum upper and maximum lower turning point depths. (The upper and lower turning point depths are functions of position for range-dependent propagation.) This choice of ordinate aids in interpreting the data, because the rays are most sensitive to the ocean at the turning point depths. Figure 11 shows that the measured travel times are greater than the predicted travel times computed using the WOA94 climatology by about 0.15 s on average, which is why delaying the predicted travel times by this amount in Figs. 7 and 8 approximately aligns the two patterns. Positive travel-time perturbations for all

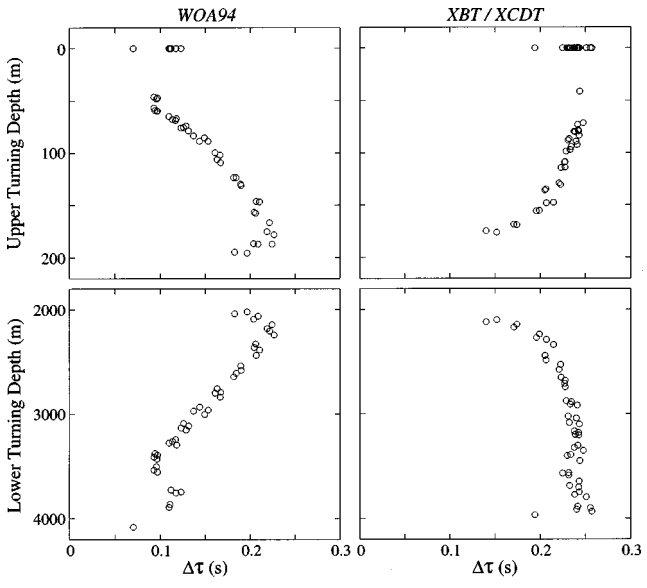

FIG. 11. Travel-time perturbations computed by subtracting the predicted travel times from the time-mean measured travel times, as derived from the beamformer output, plotted as a function of minimum upper turning depth (top) and maximum lower turning depth (bottom). The predictions were made using the sound-speed field derived from the WOA94 climatology (left) and the objectively mapped sound-speed field derived from the XBT/XCTD data combined with the WOA94 climatology (right).

rays that turn in a particular depth range suggest that sound speeds in that depth range are lower than those used to make the predictions. Because each ray turns above and below the sound-channel axis at depths with equal sound speeds (conjugate depths), the location of the sound-speed perturbation responsible for the travel-time perturbation is fundamentally ambiguous (Munk and Wunsch, 1982).

Using the time-mean travel times for the comparison assumes that, aside from internal waves and tides, changes in the sound-speed field over the duration of the experiment are small. The six-day period during which acoustic data were collected is short compared to the several-week periods typical of mesoscale variability, so this assumption is plausible. The acoustic travel times show a small, but nonzero, trend over the duration of the experiment (Fig. 10), supporting the assumption of a largely unchanging subinertial sound-speed field, at least for the purpose of identifying the ray arrivals.

Explicit error bars can be computed for the travel-time offsets relative to predictions made using the XBT/XCTD data. The error bars are a combination of the uncertainties in the measured and predicted travel times.

The computed uncertainty in the predicted travel times arises from uncertainties in the objectively mapped sound-speed field used to make the predictions (owing to the imperfect sampling of the field), to the uncertainty in the equation used to compute sound speed from temperature and salinity (± 0.05 m/s rms), and to the uncertainty in source-receiver range. The precision with which the source (1 m rms) and receiver (1.5 m rms) locations were determined using differential GPS navigation leaves an uncertainty of only about 2 m rms in the range, which is negligible compared to the other sources of uncertainty. The uncertainties in the predicted travel times were calculated using the output error covariance provided by the mapping procedure and the linearized forward problem matrix, which converts ocean parameters to travel-time perturbations. Because the objective map covered only the upper ocean, uncertainties in the deep sound-speed field were estimated from historical data.

The uncertainties in the time-mean measured travel times are a combination of the error in determining the peak arrival time due to ambient noise, internal-wave-induced travel-time fluctuations, tidally induced travel-time fluctuations, and the small travel-time trend observed over the course of the acoustic measurements. Travel-time fluctuations at tidal frequencies were fit and removed prior to forming the mean. After energy at tidal frequencies is removed, the remaining high-frequency travel-time fluctuations about a linear trend are found to be 11-19 ms rms, due primarily to internal waves. [See Colosi *et al.* (1999) for a comparison of the observed travel-time variances to predictions made assuming that the fluctuations are due to internal-wave-induced scattering.] These high-frequency travel-time fluctuations are suppressed in the mean. The trend will be discussed further in Sec. III. In this case the dominant sources of error are the travel-time trend and the uncertainty in the predicted travel times.

Surprisingly, the measured travel times are significantly offset from predictions made using the XBT/XCTD data (Fig. 11). The average time shift required to align the arrival

pattern predicted using the XBT/XCTD data and the measured arrival pattern is 0.22 s, which is significantly larger than the 0.15 s needed to align the predictions made using the WOA94 climatology with the measurements (Table I). The offset is about three times the expected rms uncertainty due to mapping errors and climatological uncertainties, although the expected rms variability of range-averaged temperature and salinity below 760-m depth is difficult to quantify. The rms difference between the measured and predicted arrival times for the optimum time shift is smaller when using the XBT/XCTD data, however, which means that the relative spacing within the arrival pattern is better predicted using the nearly concurrent environmental data (Table I). This improvement is reflected in Fig. 11, in that the travel-time offsets computed using the XBT/XCTD data are relatively independent of ray turning depth. We will return to this issue in Sec. III.

C. Surface interactions

The discussion to this point has focused on a comparison of the ray arrivals observed prior to a travel time of about 2195 s to predictions made using geometric optics. In this section, predictions made using geometric optics are compared with predictions made using a broadband adiabatic mode code to assess the adequacy of the geometric optics approximation at the long ranges and low frequencies of interest. The adiabatic mode approximation includes more complete physics than geometric optics and thus should more faithfully model reality, at least in cases for which the adiabatic approximation is valid. Boden *et al.* (1991) made similar comparisons and reported the ray approximation to be adequate for estimating travel times out to 4000-km range for frequencies above 100 Hz.

Predictions were made for a source depth of 700 m, a range of 3000 km, and a range-independent sound-speed profile typical of that found in the northeast Pacific Ocean (Colosi *et al.*, 1994). The adiabatic predictions were made for 120 modes, using the code of Dzieciuch (1993). Frequency domain predictions for a center frequency of 75 Hz and a -3-dB full bandwidth of 30 Hz were Fourier synthesized to form broadband arrival patterns in the time domain.

Comparison of calculated ray travel times with those derived from the adiabatic prediction shows that the two agree within a few milliseconds (at 3000-km range) for rays that reflect off the surface and for rays with upper turning depths well below the surface (Fig. 12). Rays with upper turning depths within a few wavelengths of the surface ($\lambda = 20$ m at 75 Hz) arrive up to 40 ms earlier in the geometric optics approximation than in the adiabatic mode approximation, however. Rays refracting near the surface, but that do not actually reflect off it, are unaffected by its presence. Modes, however, have evanescent tails that are affected by the presence of the pressure-release boundary condition at the surface, even when the modal turning depth is below the surface, slightly reducing the group speeds.

This effect is somewhat larger than the precision with which travel times can be measured, and therefore constitutes a potentially important bias for ray travel-time inversions at long ranges. For the simple range-independent geometry for which the test calculations were made, the rays turning within a few wavelengths of the surface have approximately 50 upper turning points, so the bias is roughly 1 ms per surface interaction.

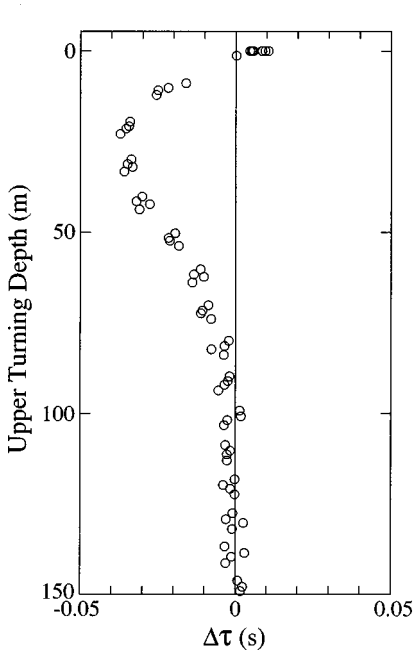

FIG. 12. Travel-time bias due to nongeometric effects for rays turning near the surface. Ray travel times minus adiabatic-mode travel times are plotted as a function of ray upper turning depth. To estimate the bias the predictions were made for a source depth of 700 m and a range of 3000 km, using a range-independent profile typical of the northeast Pacific Ocean.

The effect is expected to be relatively small for the measurements described here, however, compared to travel-time uncertainty. Surface interactions for the observed rays are confined to approximately the first 500 km of the path, because the depth of the sound-channel axis increases from the source toward the receiver, giving at most 12 surface interactions per ray, or about 12 ms bias. This small bias will be neglected when the travel times are used to estimate the sound-speed field in Sec. III. In addition, few rays have minimum upper turning depths in the upper 50 m, where the effect is most significant (Fig. 11).

This effect is not new (Murphy and Davis, 1974), but has not previously been accounted for in long-range acoustic thermometry. Boden *et al.* (1991) comment that although they found the mean differences between the ray and normal mode travel times to be small, this was not entirely due to the goodness of fit between the ray and normal-mode solutions. Their ray travel times were consistently greater than their normal-mode travel times for surface-reflected rays ($\pm 13.5°$ to $\pm 16.5°$), but the ray travel times were consistently less than the normal-mode travel times for near-surface ($\pm 11.5°$ to $\pm 13.5°$) refracted arrivals. The sign of the difference for the near-surface refracted arrivals is consistent with that found here and suggests that this effect may have been important in their simulations as well, although they did not discuss it.

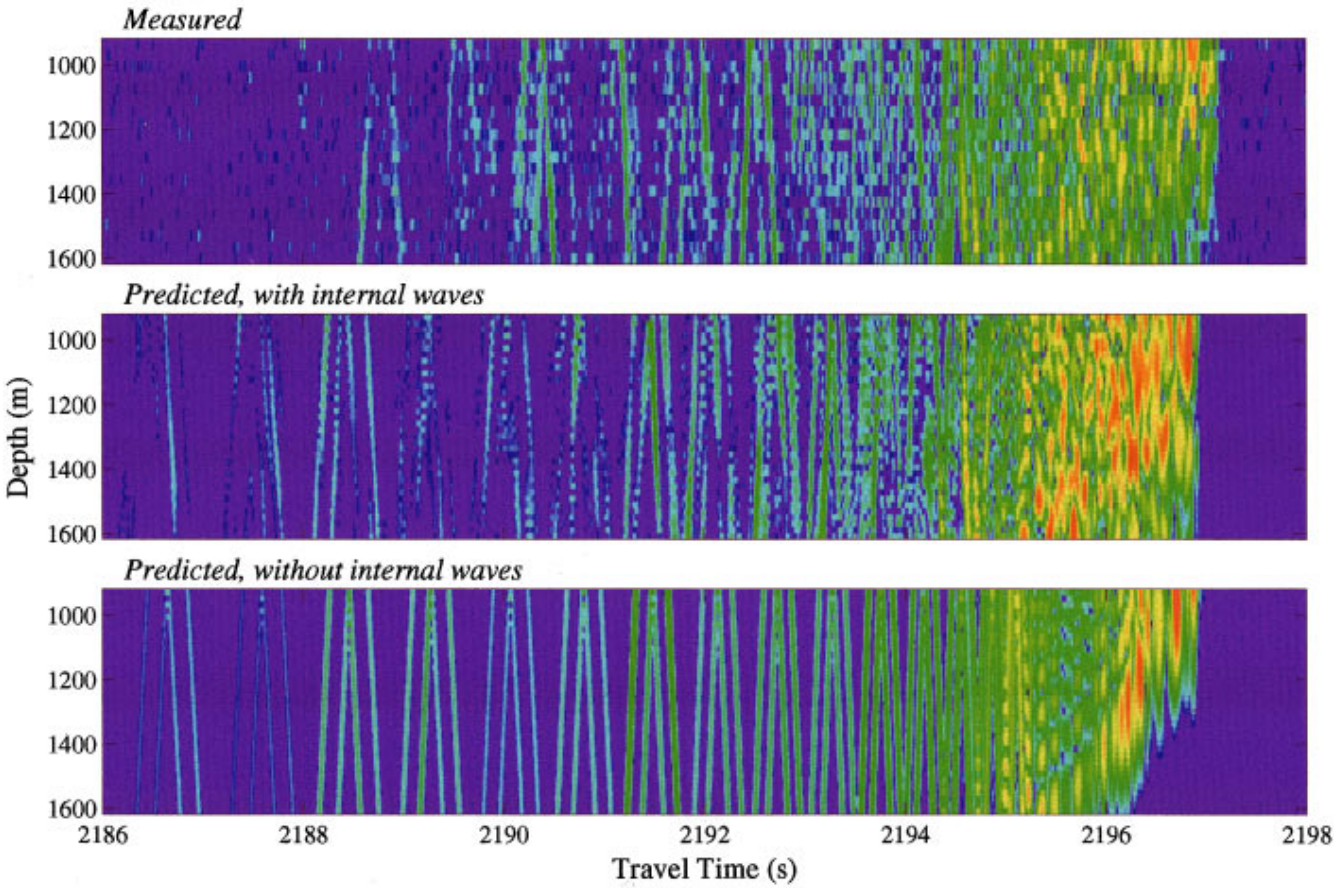

FIG. 13. Acoustic intensity as a function of travel time and hydrophone depth for one transmission (top) compared to broadband parabolic equation predictions with (middle) and without (bottom) simulated internal waves. Acoustic intensity relative to the peak intensity is plotted in decibels. The background range-dependent sound-speed field used in the simulations is shown in Fig. 6.

D. Internal-wave scattering and the pulse termination

Discreet ray arrivals are no longer evident in the measured arrival pattern for travel times greater than about 2195 s (Figs. 4 and 7). This behavior is similar to that previously observed at 1000-km range and 250-Hz center frequency (Worcester *et al.*, 1994). In that case Colosi *et al.* (1994) used broadband parabolic equation simulations to show that the observed scattering of the near-axial acoustic energy was consistent with what would be expected for propagation through an internal-wave field containing approximately one-half the energy in the standard Garrett–Munk internal-wave spectrum.

Similar broadband parabolic-equation simulations were made for the geometry of this experiment. Frequency domain predictions for a center frequency of 75 Hz and a -3-dB full bandwidth of 30 Hz were Fourier synthesized to form broadband arrival patterns in the time domain, as in the previous section. Predictions made for the sound-speed field constructed using the XBT/XCTD data (Fig. 6) give pulse terminations (i.e., the times at which the acoustic reception ends) much earlier than observed for hydrophones well below the sound-channel axis (Fig. 13). Adding a simulated internal-wave field with the standard Garrett–Munk internal-wave energy level gives a predicted arrival pattern that does not contain discreet ray arrivals after a travel time of about 2195 s and that has pulse terminations nearly independent of depth over the 900- to 1600-m-deep array aperture, as observed. Modal decompositions of similar parabolic-equation simulations at multimegameter ranges show that the propagation of the near-axial acoustic energy is generally not adiabatic, but rather that there is strong modal coupling due to the presence of internal waves (Colosi and Flatté, 1996; Colosi, 1997).

The strong scattering of near-axial energy by internal waves makes it difficult to extract useful observables for the energy arriving after about 2195 s. Rays can no longer be separated from one another, even using the vertical array to provide resolution in both time and angle. Although modal arrivals can be separated using the vertical array, internal-wave-induced modal coupling means that energy contained in a given mode at the receiver has propagated in a variety of modes, at a variety of group velocities, en route from the source to the receiver, making the interpretation of the observed group delays fundamentally ambiguous. Further, the scattered modes show significantly more time spread at the receiver than would be expected considering only modal frequency dispersion across the band of interest in the absence of internal-wave scattering, making accurate determination of the group delays difficult.

The lowest-order modes are found in the numerical simulations to be more nearly adiabatic than higher-order modes (Colosi and Flatté, 1996), however, suggesting that

their group delays (travel times) might be useful in inversions to determine the sound-speed field, increasing the vertical resolution of the resulting estimates.

The data from the vertical array can be used to estimate the amplitude of mode 1 as a function of time using least-squares techniques, even though the array aperture is at best marginal for mode isolation using conventional spatial filtering techniques (Sutton *et al.*, 1994). Unfortunately, the time history of even the lowest-order mode amplitude estimated by least squares is quite complex. Using the peak of the mode 1 amplitude to define the modal group delay gives an rms variation about the mean of 178 ms, which is much greater than the rms of about 20 ms for the observed ray travel times. This large rms variation suggests either that mode coupling due to small-scale ocean structure is more important than the simulations might suggest, or that the energy from other modes is leaking into the solution for the mode 1 amplitude because of the suboptimum array geometry. The group delay of mode 1 is thus difficult to determine.

The pulse termination at the most axial hydrophone is relatively unambiguous, however, and might be viewed as a surrogate for the group delay of adiabatic mode 1. The rms variation about a linear trend fit to the pulse termination times is 22.9 ms, which is much less than the rms variation of mode 1 as determined above and is comparable to the rms variation of the observed ray travel times. [See Colosi *et al.* (1999) for a comparison of the observed travel-time variance to a prediction made assuming that the fluctuations are due to internal-wave-induced scattering.] Even in the presence of mode coupling, no energy can travel more slowly than the energy that propagates the entire distance between source and receiver in mode 1. To the extent that any acoustic energy remains in mode 1 over the entire path, the pulse termination will reflect the travel time of that energy.

The time-mean measured travel time of the pulse termination is 398 ms greater than predicted using the WOA94 climatology, but only 75 ms greater than predicted using the objectively mapped XBT/XCTD data. Surprisingly, the use of the nearly concurrent XBT/XCTD data improves the agreement between the measured and predicted group delay for mode 1 much more significantly than their use improved the agreement between measured and predicted ray travel times, as discussed in Sec. II B. This is presumably due to a combination of effects. The midpoint of the acoustic measurements occurred on yearday 324, while the midpoint of the XBT/XCTD survey occurred four days later on yearday 328. The upper ocean can change much more rapidly than the deeper ocean, so the XBT/XCTD data can be expected to represent the state of the near-axial ocean somewhat more accurately than the state of the upper ocean at the time of the acoustic measurements. Further, and probably more important, mode 1 is sensitive to the error in near-axial sound speed integrated over the entire range. This error is reduced using the XBT/XCTD data. In contrast, the rays are sensitive both to the upper-ocean sound-speed field sampled by the XBT/XCTD measurements and to the deep sound-speed field about which the XBT/XCTD data provide no information.

III. THE INVERSE PROBLEM

In this section both the time mean and the trend in the sound-speed field between the source and receiver are estimated. The range-independent perturbation needed to bring the measured and predicted travel times into consistency is estimated first, using least squares inverse methods similar to those used to map the sound-speed field in Sec. II. The data consist of the time-mean travel times of the resolved rays and of the pulse termination at the most axial hydrophone, used as a surrogate for the group delay of mode 1. The linear trends in sound speed, temperature, and heat content over the six-day experiment are estimated next, using as data the linear trends in the travel times of the resolved rays and the pulse termination.

A. Inverting for the mean state

As was noted in Sec. II, the time-mean travel times are significantly offset from predictions based on the range-dependent sound-speed field constructed using the XBT/XCTD measurements. It is in principle impossible to construct a consistent inverse estimate for the sound-speed field between the source and receiver without increasing one or more of the *a priori* uncertainties assumed in Sec. II. The inverse estimates presented here assume a greater uncertainty in the sound-speed field below 1000-m depth than was previously estimated from historical temperature and salinity data. The notion is not that the range-averaged deep ocean temperature and salinity fields differ substantially from historically observed values, but that the equation used to compute sound speed from temperature and salinity may require further refinement at high pressure. Unfortunately, no direct measurements of the deep temperature and salinity fields were made along the acoustic path at the time of the acoustic transmissions. The estimated sound-speed perturbation below 1000-m depth therefore represents a combination of a correction to the sound-speed equation, real temperature and, to a much lesser extent, salinity perturbations, and the possible effects of travel-time biases.

To first order, the ray travel-time perturbations $\Delta\tau_i$ are weighted averages of the sound-speed perturbations $\Delta C(z)$ integrated along the unperturbed ray paths Γ_i:

$$\Delta\tau_i = -\int_{\Gamma_i} \frac{ds}{C_0^2(x,z)} \Delta C(z), \tag{4}$$

where ocean currents have been neglected and $C_0(x,z)$ is the selected reference sound-speed field. The corresponding sensitivity of the group delay of adiabatic mode 1 to the sound-speed perturbation was derived numerically.

1. Reference state

The range-dependent sound-speed field $C_0(x,z)$ constructed in Sec. II A by combining the XBT/XCTD data with the WOA94 climatology was used as the reference state (Fig. 6).

TABLE II. Vertex locations for the vertical parametrization used in the inversions.

Depth range (m)	Vertex spacing (m)
0–200	20
200–600	40
600–1400	80
1400–4000	200
4000–6000	500

2. Sound-speed perturbation model

The sound-speed perturbation field $\Delta C(z)$ was discretized (''modeled'') as a sum of range-independent vertical functions (''modes''):

$$\Delta C(z)=\sum_{j=1}^{M} a_j F_j^C(z), \tag{5}$$

where a_j are the model parameters, which were assumed to be uncorrelated. In anticipation of the next section, the vertical sound-speed modes were derived by first representing the temperature perturbation field as a sum of range-independent vertical functions

$$\Delta T(z)=\sum_{j=1}^{M} a_j F_j^T(z). \tag{6}$$

The XBT EOFs used previously are not expected to represent arbitrary range-averaged offsets, and thus are not a good choice for upper ocean functions in this application. The historical data base is too limited a sample to provide reliable estimates of the vertical covariance function expected for range-averaged temperature perturbations. Instead, linear splines (piecewise linear segments) were used, with the knot spacing adjusted in accord with rough estimates of the vertical length scales,

$$\begin{aligned}
&F_j^T(z)=0, \quad z<z_{j-1},\\
&F_j^T(z)=\frac{(z-z_{j-1})}{(z_j-z_{j-1})}, \quad z_{j-1}\leqslant z\leqslant z_j,\\
&F_j^T(z)=\frac{(z_{j+1}-z)}{(z_{j+1}-z_j)}, \quad z_j<z\leqslant z_{j+1},\\
&F_j^T(z)=0, \quad z_{j+1}<z.
\end{aligned} \tag{7}$$

Forty-eight vertical functions were used, with vertex spacings that increase with increasing depth, reflecting our prejudice that vertical scales become larger at greater depths (Table II). A range-independent model was used in this case in part because little range-dependent information is expected from the travel times and in part for simplicity.

Sound-speed and heat-content modes were constructed for each temperature mode by treating the temperature modes as perturbations to a reference temperature profile constructed by averaging the WOA94 climatology along the acoustic path. Each temperature perturbation (with a maximum amplitude of 0.1 °C for linearity) was added to the reference temperature profile, and sound speed and heat content were calculated for the perturbed profile using the range-averaged salinity from the WOA94 climatology. Heat content was integrated upward from 4200-m depth, which was chosen because this depth is below the deepest ray turning point,

$$H(z)=\rho C_p \int_{-D}^{z} T(z')dz', \tag{8}$$

where H has units of energy per unit area, $\rho=1024\ \mathrm{kg/m^3}$ is the density of seawater, $C_p=3996\ \mathrm{J/(kg\,°C)}$ is the specific heat of seawater, $T(z)$ is the range-averaged temperature profile, and $D=4200$ m. The reference sound speed or heat content was then subtracted from the perturbed profile, as appropriate, and the resultant perturbation used as the sound speed or heat content analog of the vertical temperature mode.

Only the sound-speed perturbation was computed for the mean state, so this rather elaborate procedure was not necessary. But sound-speed, temperature, and heat content perturbations will be computed in the next section for the trend. This procedure uses a single set of model parameters to provide consistent estimates for all three perturbations, assuming no salinity perturbations.

Finally, the expected range-average temperature variability as a function of depth, relative to the reference state constructed using the XBT/XCTD data, is estimated to be 0.12 °C rms at the surface, decreasing nearly linearly to 0.05 °C rms at 1000-m depth. The variability was assumed to remain constant at 0.05 °C rms below 1000 m. A number of considerations went into this estimate.

Above 760-m depth the dominant source of temperature uncertainty in the range-average field is the four-day separation between the midpoint of the acoustic measurements and the midpoint of the XBT/XCTD measurements. A rough guess at the possible magnitude of the temperature change was made by assuming that the range-averaged temperature could change 1 °C in 30 days (consistent with possible mesoscale variability), giving a change of 0.12 °C in the 3.6 days between the midpoints of the acoustic and XBT/XCTD measurements. The XBT/XCTD measurements themselves provide a rather tight constraint on the quasi-instantaneous range-average field. The combination of measurement error and internal-wave-induced temperature fluctuations is estimated to give a rms temperature uncertainty of about 0.1 °C for a single measurement. In the range average over 111 profiles this uncertainty is reduced by a factor of approximately 10 to about 0.010 °C. The bias of the XBT temperatures is not expected to exceed 0.020 °C.

At depths below those for which there are XBT/XCTD data, the rms temperature uncertainty in the range average deduced from historical data is rather small. At 3000-m depth, for example, the rms temperature variability is about 0.025 °C. If one assumes a horizontal scale of 100 km, the uncertainty in the range average over the 3250-km-long path is then only about 0.004 °C. The estimated rms uncertainty in the equation used to convert temperature and salinity to sound speed is 0.05 m/s (Del Grosso, 1974; Spiesberger, 1993; Dushaw *et al.*, 1993; Meinen and Watts, 1997), corresponding to a rms temperature uncertainty of about 0.011 °C. Because the separation between the source and receiver was not measured nearly as precisely in previous

field tests of the sound-speed equation as in this experiment, however, it is possible that an error in the sound-speed equation was previously incorrectly attributed to an error in the range. The best previous field test of the sound-speed equation had range uncertainties of about 70 m, for example (Dushaw *et al.*, 1993). To account for the uncertainty in the sound-speed equation, the *a priori* rms temperature uncertainty was increased to 0.05 °C below 1000-m depth, which allowed consistent inverse estimates.

3. Data

The data are the travel-time perturbations $\Delta\tau_i$ computed by subtracting the travel times predicted using the XBT/XCTD data from the time-mean measured travel times (Fig. 11). The travel-time uncertainties are a combination of measurement error due to ambient noise, internal-wave-induced travel-time fluctuations, and travel-time fluctuations due to mesoscale variability unresolved by the XBT/XCTD data. The high-frequency travel-time fluctuations about linear trends fit to the ray data are 11-19 ms rms (Colosi *et al.*, 1999). The uncertainty in the time-mean ray travel times is then about 3 ms rms. More significant is the travel-time uncertainty associated with mesoscale range dependence that is not resolved by the XBT/XCTD data and not included in the sound-speed perturbation model. If we assume that travel-time variability between rays with nearly the same lower turning points must be due to unresolved horizontal variability, Fig. 11 suggests that mesoscale-induced travel-time fluctuations are less than 20 ms rms. The uncertainty in the time-mean ray travel times was therefore rather conservatively taken to be 20 ms rms. Finally, the uncertainty in the mean pulse termination travel time is taken to be 100 ms rms, considerably larger than the measured variability of about 23 ms rms, to reflect the uncertainty in interpreting the pulse termination as a surrogate for adiabatic mode 1 and to allow for any internal-wave-induced group delay bias.

Any travel-time biases have been ignored in the inversions, other than to increase the travel-time uncertainties. Assuming a standard Garrett–Munk internal-wave spectrum Colosi and Flatté (1996) found biases of about -10 ms at 3-Mm range from their simulations for a case similar, but not identical, to the one examined here. A negative bias means that the ray is predicted to arrive earlier (have a shorter travel time) in the presence of internal waves than in their absence. Negative biases would slightly increase the discrepancy in Fig. 11 because the predictions would have even shorter travel times, making the measured minus predicted travel times more positive. Colosi *et al.* (1999) find that the observed travel-time variances for the experiment described here are consistent with predictions assuming that the internal-wave field has one-half of the standard Garrett–Munk energy level. Using this energy level would reduce the biases in the simulations from -10 to -5 ms. Further, the observed pulse spreads are only 0–5 ms (Colosi *et al.*, 1999). The pulse spread and bias are expected to be of the same order, and so this result is consistent with the biases found in the simulations. The biases of the rays are therefore comparable to or less than the assumed random errors. Nonetheless, the biases may still affect the inverse estimates if all of the ray travel times have similar, systematic biases.

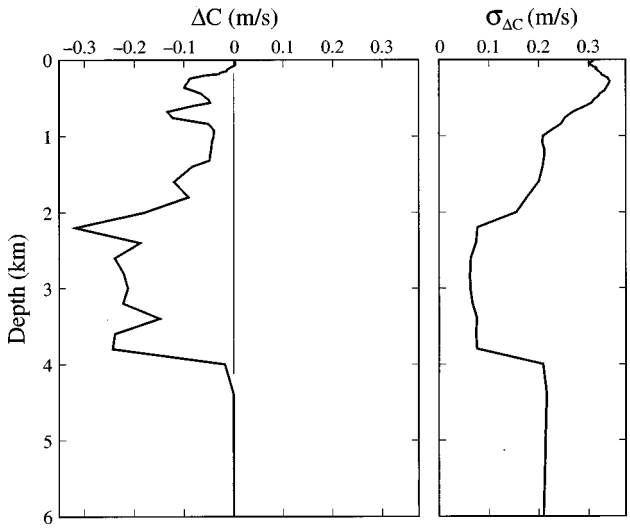

FIG. 14. Range-independent sound-speed perturbation and the associated rms uncertainty as a function of depth.

The group delays of the lowest-order normal modes are found to be more biased by internal-wave-induced scattering than are the travel times of the steep rays. Colosi and Flatté (1996) found from their simulations that the bias for acoustic mode 1 grows as the square of the range and is about -45 ms at 3-Mm range for the sound-speed profile they used and for the standard Garrett–Munk internal-wave energy level. Using one-half of the standard Garrett–Munk energy level in the simulations would reduce the bias from -45 to -22.5 ms. This bias is substantially smaller than the group delay uncertainty of 100 ms assumed here.

4. Results

Finally, inverting the time-mean travel-time perturbations in Fig. 11 for the a_j gives the mean sound-speed perturbation profile shown in Fig. 14. The linear travel-time residuals are consistent with the *a priori* assumptions (Table III). Retracing rays through the perturbed sound-speed field $C_0(x,z)+\Delta C(z)$ gives travel times consistent with the measurements, indicating that the reference state selected is sufficiently close to the true state for the inversions to be linear. No iterations of the inverse were done.

The estimated sound-speed perturbations are small above about 1000-m depth, reflecting the constraints imposed by the XBT/XCTD data. The estimated perturbation is

TABLE III. Unweighted travel-time perturbations (rms) for the rays and acoustic modes 1–20 before (data) and after (residuals) inversion. The data are travel-time perturbations relative to the reference state. The residuals are linear estimates of the travel-time perturbations relative to the perturbed sound-speed profile. The values for acoustic mode 1 are shown separately. Only mode 1 was used in the inversion.

	Data (s)	Residuals (s)
Ray travel times (rms)	0.226	0.028
Modal group delays (rms)	0.283	0.228
Mode 1 group delay	0.075	−0.020

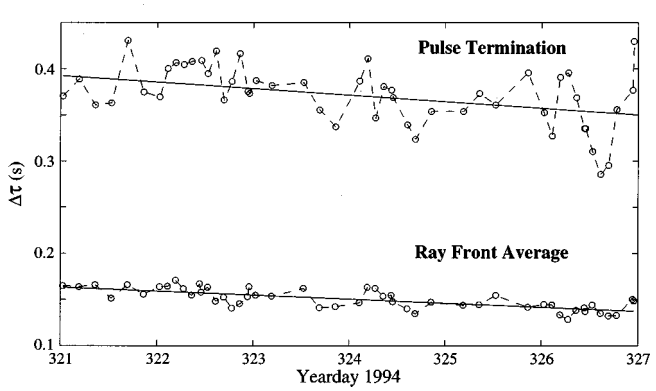

FIG. 15. Travel-time perturbations computed by subtracting the predicted travel times for the WOA94 climatology from the measured travel times, as derived from the pulse termination (top) and the beamformer output for the identified ray wave fronts (bottom). The lower curve is an average over all of the identified wave fronts. A straight-line fit gives a trend of -7.1 ms/day for the pulse termination and -4.4 ms/day for the ray front average.

largest, about -0.2 ± 0.05 m/s, between 2000 and 4000 m. If the sound-speed perturbation were due entirely to an error in the sound-speed equation, the correction would be three to four times the *a priori* uncertainty in the equation. (Theoretical corrections to the sound-speed equation due to variations in the relative composition of salts in the ocean and due to the dependence of sound speed on acoustic frequency are smaller than 0.05 m/s (Dushaw *et al.*, 1993)). If the sound-speed perturbation were entirely due to temperature, the corresponding temperature perturbation would be $-0.044\pm0.011\,^{\circ}$C, which is 10-11 times the *a priori* range-average temperature uncertainty. Both effects may well be important, although it seems probable that the dominant effect is an error in the sound-speed equation. Accurate deep hydrographic data taken during the time of the acoustic transmissions would be needed to resolve definitively the issue.

One important conclusion from these results is that once the sound-speed equation is better determined, the absolute range-average temperature at depth can be determined acoustically with an estimated uncertainty of about 10 millidegrees, neglecting any effects due to salinity.

B. Inverting for the trend

In the application to climate studies, the important consideration is the precision with which temperature *changes*, rather than the absolute temperature, can be measured. The measured travel times of both the ray wave fronts and the pulse termination slowly decreased over the six days of the experiment (Fig. 15).

To first order, the time derivative of the travel-time perturbation for ray i is

$$\frac{d}{dt}(\Delta\tau_i)=-\int_{\Gamma_i}\frac{ds}{C_0^2(x,z)}\frac{d}{dt}[\Delta C(z)]. \tag{9}$$

The sensitivity of the time derivatives of the travel-time perturbations to the time derivatives of the sound-speed perturbations is identical to that of the travel-time perturbations themselves to the sound-speed perturbations.

1. Reference state

The range-dependent, time-independent, sound-speed field $C_0(x,z)$ constructed by combining the XBT/XCTD data with the WOA94 climatology was the reference state, as in the preceding section.

2. Sound-speed trend perturbation model

The time derivative of the sound-speed perturbation field $d[\Delta C(z)]/dt$ was modeled as a sum of the same range-independent vertical modes as in the preceding section, so the vertical modes used previously now represent the time rate of change of the field,

$$\frac{d}{dt}[\Delta T(z)]=\sum_{j=1}^{M} b_j F_j^T(z), \tag{10}$$

and

$$\frac{d}{dt}[\Delta C(z)]=\sum_{j=1}^{M} b_j F_j^C(z), \tag{11}$$

where b_j are the model parameters.

The rms variability in the temperature trend was taken very arbitrarily to be $0.030\,^{\circ}$C/day at the surface, corresponding to a trend of $1\,^{\circ}$C/month, dropping nearly linearly to $0.002\,^{\circ}$C/day rms at 1000-m depth and $0.001\,^{\circ}$C/day rms at 6000-m depth.

3. Data

The data were the linear travel-time trends $d(\Delta\tau_i)/dt$ computed from least-squares fits to the travel-time series (Fig. 15). The ray-mean travel times of all of the resolved ray arrivals decreased by 4.4 ms/day, with a rms variation of 5.9 ms rms about the linear trend. The trends from separate linear fits to each ray-travel-time series were used as data in the inverse. The travel time of the pulse termination decreased somewhat more rapidly, by 7.1 ms/day, with a rms variation of 22.9 ms about the linear trend, as reported previously. The uncertainty in the individual linear trends was taken to be 3 ms/day rms, independent of ray path, due to the observed scatter around the individual trends.

4. Results

Finally, inverting the travel-time trends for the b_j gives the sound-speed perturbation trend shown in Fig. 16. The temperature and heat-content perturbation trends are computed from the same b_j because of the way in which the sound-speed perturbation trend model was developed. Sound speed, temperature, and heat content are all increasing, leading to shorter travel times. The sound-speed and temperature trends both show positive perturbations above 1000-m depth and between 2000- and 4000-m depth. The uncertainty in the temperature estimate is approximately $0.001\,^{\circ}$C/day below 1000-m depth, increasing to about $0.030\,^{\circ}$C/day at the surface (i.e., the original uncertainty at the surface). The total temperature change over the six-day period can therefore be estimated with an uncertainty of about $0.006\,^{\circ}$C below 1000-m depth, corresponding to a sound-speed uncertainty of about 0.03 m/s. Not unexpectedly, the total sound-speed

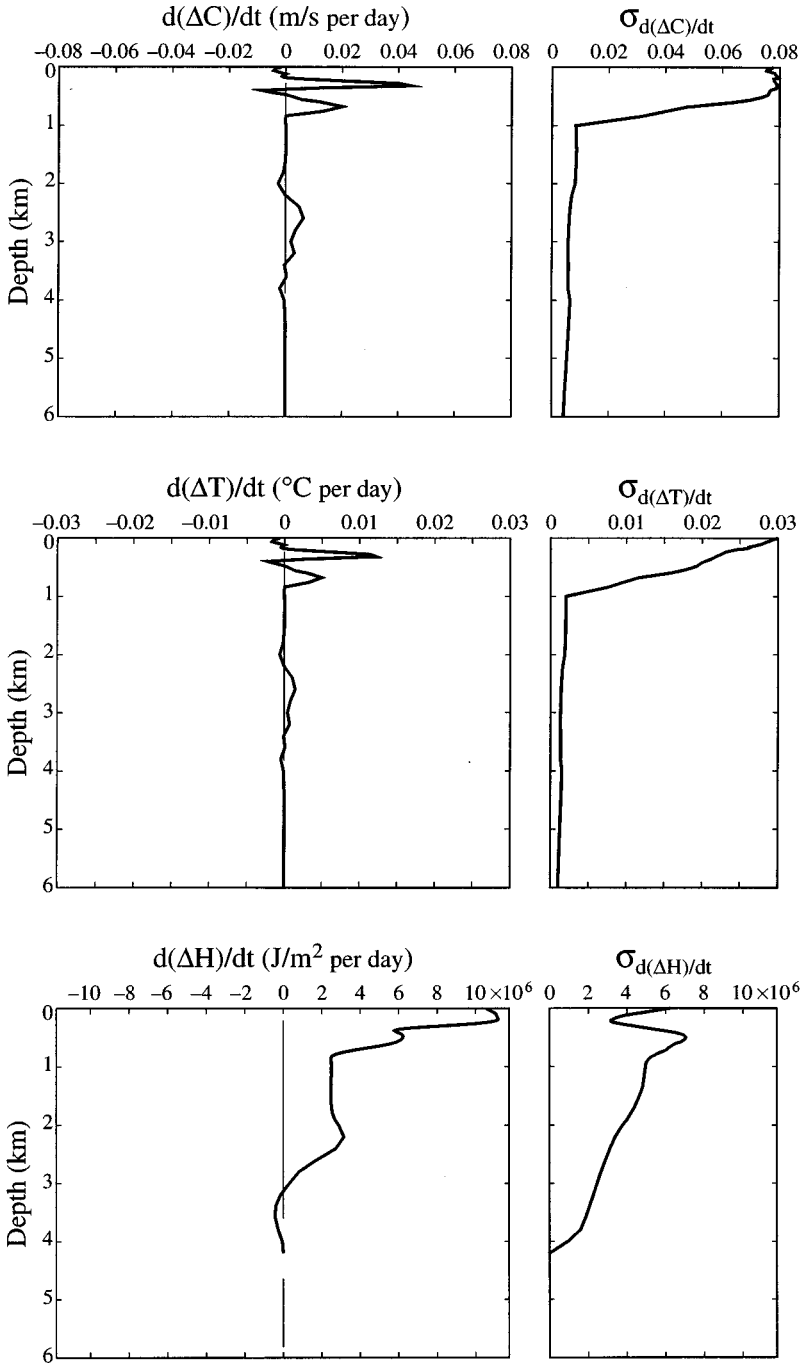

FIG. 16. Rate of change of sound speed, temperature, and heat content and the associated rms uncertainties as a function of depth over the duration of the experiment, as inferred from the linear trends shown in Fig. 15.

change over the six days can be estimated with an uncertainty roughly comparable to that with which the absolute sound-speed change could be determined in the previous section.

The correlated perturbations near the surface and between 2000 and 4000 m are a reflection of up–down ambiguity (Munk and Wunsch, 1982). Sound-speed perturbations above and below the sound-channel axis affect the ray travel times similarly, so the inverse estimate distributes the total variance over depth in accord with the *a priori* sound-speed trend uncertainty profile. This effect was less evident in the estimate of the mean perturbation because the XBT/XCTD data constrained the inverse estimate above the axis. There is no similar constraint on the trend. The inverse estimate uncertainty above and below the axis is correlated, however, so the uncertainty in the depth integral of heat content is less. The reduction in the uncertainty of the heat content trend just beneath the surface, with a minimum at about 100-m depth, occurs where the integral includes both the upper and lower turning points of most of the ray paths.

IV. DISCUSSION

The ATOC Acoustic Engineering Test provides a stringent test of our ability to predict absolute travel times because the XBT/XCTD data constrain the sound-speed field in the upper ocean, where maximum variability is expected, and because the range between the source and receiver is known to within a few meters. Somewhat surprisingly, the measured and predicted absolute travel times are found to be

offset by more than is consistent with *a priori* ocean variability estimates derived from climatology. The discrepancy is probably due to an error in the sound-speed equation at high pressures, as simulations and observations of pulse time spread, τ_0, strongly suggest that the biases in the measured travel times are minimal. The absolute ray arrival travel times can be inverted to give estimates of sound speed with an uncertainty of about 0.05 m/s below the sound-channel axis, which is about 20% of the *a priori* variability. The uncertainty in the equation used to convert temperature and salinity to sound speed makes conversion of these absolute sound-speed estimates to temperature uncertain. More important, the trend in temperature with time can be estimated with an uncertainty of about 0.001 °C/day below the sound-channel axis, which is about one-half of the *a priori* variability of 0.002 °C/day.

The vertical resolution of the estimates is limited by internal-wave-induced scattering for this acoustic path. Ray arrivals from paths with minimum upper turning depths above about 200 m were resolvable, identifiable, and stable. Rays with upper turning depths deeper than about 200 m were scattered by internal-wave-induced sound-speed fluctuations. Inversions using ray travel times together with the time of the near-axial pulse termination as a surrogate for the group delay of adiabatic mode 1 therefore have limited vertical resolution, with information from the ray arrivals concentrated above 200-m depth and at the corresponding conjugate depths of 2000 to 4000 m and information from the pulse termination concentrated near axial depth. Other data suggest that this result is strongly dependent on the sound-speed profile, however, and that measurements in other geographic regions can be expected to have different resolution properties. Acoustic receptions at about 1000-km range in the northwestern Atlantic Ocean (Spiesberger *et al.*, 1980), for example, contain resolvable, identifiable, and stable ray arrivals with a much wider range of upper turning point depths than are observed at similar range in the northeastern Pacific Ocean (Dushaw *et al.*, 1993; Worcester *et al.*, 1994).

Our conclusion is that it is feasible to use acoustic transmissions to at least 3-Mm range to make high-precision measurements of range-averaged profiles of ocean sound speed and of changes in ocean temperature and heat content. Subsequent to the ATOC Acoustic Engineering Test, the ATOC project has in fact used acoustic sources and receivers in the Northeast Pacific Ocean to obtain travel-time data for many ray paths. These data have been combined with satellite altimeter measurements and a numerical ocean general circulation model using data assimilation methods to produce improved estimates of the ocean state, including heat content and fluxes (ATOC Consortium, 1998).

ACKNOWLEDGMENTS

Many people contributed to the fielding and analysis of this experiment, including S. Abbott, L. Day, K. Hardy, D. Horwitt, A. Marshall, D. Peckham, A. Rivera, and R. Truesdale from the Scripps Institution of Oceanography (SIO); J. Kemp, E. Scheer, and K. von der Heydt from the Woods Hole Oceanographic Institution (WHOI); and S. Anderson, R. Drever, F. Karig, S. Leach, V. Miller, L. Olson, D. Reddaway, R. Ryan, R. Stein, J. Watson, and S. Weslander from the Applied Physics Laboratory at the University of Washington. The crew of R/P FLIP and the support personnel at the Marine Physical Laboratory of the Scripps Institution of Oceanography were exceptionally helpful. The crews of M/V Recovery One, R/V Moana Wave, and CSS John P. Tully all contributed to the success of the experiment. This work was supported largely by the Strategic Environmental Research and Development Program through Defense Advanced Research Projects Agency (DARPA) Grant No. MDA972-93-1-0003. Additional support was provided at SIO by the Office of Naval Research (ONR) through Grant No. N00014-97-1-0258. J. Colosi wishes to acknowledge support from an ONR Young Investigator Award, from the J. Lamar Worzel Assistant Scientist Fund, and from the Penzance Endowed Fund in support of scientific staff at WHOI.

ATOC Consortium (**1998**). Baggeroer, A. B., Birdsall, T. G., Clark, C., Colosi, J. A., Cornuelle, B. D., Costa, D., Dushaw, B. D., Dzieciuch, M., Forbes, A. M. G., Hill, C., Howe, B. M., Marshall, J., Menemenlis, D., Mercer, J. A., Metzger, K., Munk, W., Spindel, R. C., Stammer, D., Worcester, P. F., and Wunsch, C., ''Ocean climate change: Comparison of acoustic tomography, satellite altimetry, and modeling,'' Science **281**, 1327–1332.

ATOC Instrumentation Group (**1995**). Howe, B. M., Anderson, S. G., Baggeroer, A. B., Colosi, J. A., Hardy, K. R., Horwitt, D., Karig, F. W., Leach, S., Mercer, J. A., Metzger, K., Jr., Olson, L. O., Peckham, D. A., Reddaway, D. A., Ryan, R. R., Stein, R. P., von der Heydt, K., Watson, J. D., Weslander, S. L., and Worcester, P. F. ''Instrumentation for the Acoustic Thermometry of Ocean Climate (ATOC) prototype Pacific Ocean network,'' *OCEANS'95 Conference Proceedings*, San Diego, CA, 9–12 October 1995, pp. 1483–1500.

Baggeroer, A. B., Sperry, B., Lashkari, K., Chiu, C.-S., Miller, J. H., Mikhalevsky, P. N., and von der Heydt, K. (**1994**). ''Vertical array receptions of the Heard Island transmissions,'' J. Acoust. Soc. Am. **96**, 2395–2413.

Boden, L., Bowlin, J. B., and Spiesberger, J. L. (**1991**). ''Time domain analysis of normal mode, parabolic, and ray solutions of the wave equation,'' J. Acoust. Soc. Am. **90**, 954–958.

Bowlin, J. B., Spiesberger, J. L., Duda, T. F., and Freitag, L. (**1993**). ''Ocean acoustical ray-tracing software RAY,'' Woods Hole Oceanographic Tech. Rep., WHOI-93-10.

Chen, C.-T., and Millero, F. J. (**1977**). ''Speed of sound in seawater at high pressures,'' J. Acoust. Soc. Am. **62**, 1129–1135.

Colosi, J. A. (**1997**). ''Random media effects in basin-scale acoustic transmissions,'' Proceedings of the 1997 Áha Hulikoá Winter Workshop, pp. 157–166.

Colosi, J. A., and Flatté, S. M. (**1996**). ''Mode coupling by internal waves for multimegameter acoustic propagation in the ocean,'' J. Acoust. Soc. Am. **100**, 3607–3620.

Colosi, J. A., Flatté, S. M., and Bracher, C. (**1994**). ''Internal-wave effects on 1000-km oceanic acoustic pulse propagation: Simulation and comparison with experiment,'' J. Acoust. Soc. Am. **96**, 452–468.

Colosi, J. A., Scheer, E. K., Flatté, S. M., Cornuelle, B. D., Dzieciuch, M. A., Munk, W. H., Worcester, P. F., Howe, B. M., Mercer, J. A., Spindel, R. C., Metzger, K., Birdsall, T. G., and Baggeroer, A. B. (**1999**). ''Comparisons of measured and predicted acoustic fluctuations for a 3250-km propagation experiment in the eastern North Pacific Ocean,'' J. Acoust. Soc. Am. **105**, 3202–3218.

Cornuelle, B. D., Worcester, P. F., Hildebrand, J. A., Hodgkiss, Jr., W. S., Duda, T. F., Boyd, J., Howe, B. M., Mercer, J. A., and Spindel, R. C. (**1993**). ''Ocean acoustic tomography at 1000-km range using wave fronts measured with a large-aperture vertical array,'' J. Geophys. Res. **98**, 16365–16377.

Del Grosso, V. A. (**1974**). ''New equation for the speed of sound in natural waters (with comparisons to other equations),'' J. Acoust. Soc. Am. **56**, 1084–1091.

Duda, T. F., Flatté, S. M., Colosi, J. A., Cornuelle, B. D., Hildebrand, J. A., Hodgkiss, Jr., W. S., Worcester, P. F., Howe, B. M., Mercer, J. A., and Spindel, R. C. (**1992**). ''Measured wave-front fluctuations in 1000-km

pulse propagation in the Pacific Ocean,'' J. Acoust. Soc. Am. **92**, 939–955.
Dushaw, B. D., Worcester, P. F., Cornuelle, B. D., and Howe, B. M. (**1993**). ''On equations for the speed of sound in seawater,'' J. Acoust. Soc. Am. **93**, 255–275.
Dzieciuch, M. A. (**1993**). ''A spectral method for calculation of ocean acoustic normal modes using Chebyshev polynomials,'' J. Acoust. Soc. Am. **94**, 1785.
Howe, B. M., Mercer, J. M., Spindel, R. C., Worcester, P. F., Hildebrand, J. A., Hodgkiss, Jr., W. S., Duda, T. F., and Flatté, S. M. (**1991**). ''SLICE89: A single slice tomography experiment,'' in *Ocean Variability and Acoustic Propagation*, Proceedings of the Workshop on Ocean Variability and Acoustic Propagation, La Spezia, Italy, 4–8 June 1990, edited by J. Potter and A. Warn Varnas (Kluwer Academic, Dordrecht), pp. 81–86.
Levitus, S. (**1982**). ''Climatological Atlas of the World Ocean,'' NOAA Professional Paper 13.
Levitus, S., and Boyer, T. P. (**1994**). *World Ocean Atlas 1994, Volume 4: Temperature*, NOAA Atlas NESDIS 4.
Levitus, S., Burgett, R., and Boyer, T. P. (**1994**). *World Ocean Atlas 1994, Volume 3: Salinity*, NOAA Atlas NESDIS 3.
Meinen, C. S., and Watts, D. R. (**1997**). ''Further evidence that the sound-speed algorithm of Del Grosso is more accurate than that of Chen and Millero,'' J. Acoust. Soc. Am. **102**, 2058–2062.
Menemenlis, D., Fieguth, P., Wunsch, C., and Willsky, A. (**1997**). ''Adaptation of a fast optimal interpolation algorithm to the mapping of oceanographic data,'' J. Geophys. Res. **102**, 10573–10584.
Millero, F. J., and Li, X. (**1994**). ''Comments on 'On equations for the speed of sound in seawater' [J. Acoust. Soc. Am. **93**, 255–275 (1993)],'' J. Acoust. Soc. Am. **95**, 2757–2759.
Munk, W., and Wunsch, C. (**1982**). ''Up-down resolution in ocean acoustic tomography,'' Deep-Sea Res. **29**, 1415–1436.
Munk, W., Worcester, P., and Wunsch, C. (**1995**). *Ocean Acoustic Tomography* (Cambridge U.P., Cambridge).
Munk, W. H., Spindel, R. C., Baggeroer, A. B., and Birdsall, T. G. (**1994**). ''The Heard Island Feasibility Test,'' J. Acoust. Soc. Am. **96**, 2330–2342.
Murphy, E. L., and Davis, J. A. (**1974**). ''Modified ray theory for bounded media,'' J. Acoust. Soc. Am. **56**, 1747–1760.
National Geophysical Data Center (**1988**). ''ETOPO-5 bathymetry/topography data,'' Data Announcement 88-MGG-02, Natl. Oceanic and Atmos. Admin., U.S. Department of Commerce, Boulder, CO.
Sandwell, D. T., and Smith, W. H. F. (**1997**). ''Marine gravity from Geosat and ERS-1 altimetry,'' J. Geophys. Res. **102**, 10039–10054.
Smith, W. H. F., and Sandwell, D. T. (**1994**). ''Bathymetric prediction from dense satellite altimetry and sparse shipboard bathymetry,'' J. Geophys. Res. **99**, 21803–21824.
Smith, W. H. F., and Sandwell, D. T. (**1997**). ''Global sea floor topography from satellite altimetry and ship depth soundings,'' Science **277**, 1956–1962.
Spiesberger, J. L. (**1993**). ''Is Del Grosso's sound-speed algorithm correct?'' J. Acoust. Soc. Am. **93**, 2235–2237.
Spiesberger, J. L., and Metzger, K. (**1991**). ''Basin-scale tomography: A new tool for studying weather and climate,'' J. Geophys. Res. **96**, 4869–4889.
Spiesberger, J. L., and Tappert, F. D. (**1996**). ''Kaneohe acoustic thermometer further validated with rays over 3700 km and the demise of the idea of axially trapped energy,'' J. Acoust. Soc. Am. **99**, 173–184.
Spiesberger, J. L., Spindel, R. C., and Metzger, K. (**1980**). ''Stability and identification of ocean acoustic multipaths,'' J. Acoust. Soc. Am. **67**, 2011–2017.
Spiesberger, J. L., Terray, E., and Prada, K. (**1994**). ''Successful ray modeling of acoustic multipaths over a 3000-km section in the Pacific,'' J. Acoust. Soc. Am. **95**, 3654–3657.
Sutton, P., Morawitz, W. M. L., Cornuelle, B. D., Masters, G., and Worcester, P. F. (**1994**). ''Incorporation of acoustic normal mode data into tomographic inversions in the Greenland Sea,'' J. Geophys. Res. **99**, 12487–12502.
Worcester, P. F., Cornuelle, B. D., Hildebrand, J. A., Hodgkiss, Jr., W. S., Duda, T. F., Boyd, J., Howe, B. M., Mercer, J. A., and Spindel, R. C. (**1994**). ''A comparison of measured and predicted broadband acoustic arrival patterns in travel time-depth coordinates at 1000-km range,'' J. Acoust. Soc. Am. **95**, 3118–3128.